




Impact of high NiO content on the structural, optical, and dielectric properties of calcium lithium silicate glasses

S. Ibrahim¹, H. A. Abo-Mosallam¹, Ebrahim A. Mahdy^{1,*} , and Gamal M. Turkey²

¹Glass Research Department, National Research Centre, 33El-Buhouth St, Dokki 12622, Cairo, Egypt

²Department of Microwave Physics & Dielectrics, National Research Centre, 33El-Buhouth St, Dokki 12622, Cairo, Egypt

Received: 26 January 2022

Accepted: 5 March 2022

Published online:
26 March 2022

© The Author(s) 2022

ABSTRACT

Glasses with the composition $(11.5 - x) \text{CaO} - 23.5\text{Li}_2\text{O} - 65\text{SiO}_2 \cdot x \text{NiO}$ mol. % ($0 \leq x \leq 11.5$) were synthesized by melt-quenching method. A number of physical parameters have been established. The refractive index and energy gap were also used to estimate the metallization criterion, where these glasses have shown values fallings between high (insulators) and low (metals), indicating that they are semiconductors. The XRD pattern shows the amorphous nature of investigated glasses. A number of spectroscopic analyses of the studied glasses were performed, in relation to NiO content, including Fourier transform infrared (FTIR) and UV-Visible diffuse reflectance spectroscopy (DRS). Due to compositional changes, FTIR measurements have revealed structural changes in the glass network. Furthermore, with increasing NiO content, the asymmetrical bands of silicate units increase. The creation of Ni-O-Si bonds in the silicate matrix has been attributed to the introducing heavier Ni^{+2} as $[\text{NiO}_4]^{2-}$ tetrahedral species in substitution of the lighter silicon ion in the $[\text{SiO}_4]^{4-}$ network, but it could also operate as a network modifier in glass materials. The Ni^{2+} ion may have behaved as a network intermediary, causing more compact structure. The mechanism of charge transfer in the glass compositions under investigation is studied using broadband dielectric spectroscopy. For the first time, the relationship between the hopping time of free ions and dc conductivity is illustrated. All of the glasses under investigation have the same charge transport mechanism. The results suggest the semiconducting nature of these glasses.

Address correspondence to E-mail: emahdy10@yahoo.com; ea.mahmoud@nrc.sci.eg

1 Introduction

Lithium based-silicate glasses are widely recognized as photosensitive glasses [1]. They are thermally, chemically, and mechanically stable, making them a perfect host for transition metal ions with intense luminescence in the visible region [1, 2]. In amorphous matrices, nickel ions are very stable and mainly occupy octahedral sites. The spectroscopic properties of Ni^{2+} ions in glasses are remarkable due to their high stability, and various intensive investigations into these materials are present in the literature [3–5].

In glass materials, a portion of Ni^{2+} ions may occupy tetrahedral positions, besides octahedral occupation. Quantitative properties of modifiers and glass formers, as well as their field strength, the size of the ions in the glass matrix, modifier cation motion, and other factors, all influence the concentration of ions in tetrahedral or octahedral sites [6]. The octahedral nickel ions function as modifiers, generating structural flaws, whereas the tetrahedral ions combine with the basic glass network. The physical properties of the host glass material, particularly its electrical properties, are likely to be influenced by the movement of nickel ions between these two sites [7]. The electron configuration of the transition metal nickel ions causes the shell layer being $3d^8 4s^0$, transitions among Ni^{2+} ions d orbits are more sensitive to matrix changes [8].

Nickel oxide has been the subject of several scientific studies, particularly due to its remarkable optical, electrical, and magnetic properties [9]. NiO is a p -type semiconductor prototype with a 3.6–4.0 eV broad bandgap [10]. Before being employed in perovskite solar cells (PSCs), nickel oxide was used as the p -type hole transport layers (HTL) in dye-sensitized solar cells (DSSCs) and organic photovoltaics (OPV). NiOx has a high transparency due to its wide bandgap (3.6 eV), deep valence band (– 5.2 to – 5.4 eV), and high carrier mobility ($0.1 \text{ cm}^2/\text{Vs}$), as well as good light, heat, and moisture stability, making it a good candidate for hole transport layers (HTL) in perovskite solar cells (PSCs). Using a low-temperature combustion technique, copper-doped NiOx (Cu:NiOx) achieved efficiencies of over 17.8%, outperforming the traditional sol-gel-derived high-temperature Cu:NiOx PCE of 15.5%. Thus, various elements such as Cu, Li, Mg, Cs, and Co can be

doped into NiOx to improve conductivity and PSC efficiency by lowering interfacial resistance at the HTL/perovskite interface [11].

The electronic features of NiO have benefited anodes for lithium-ion batteries, electrochromic coatings, solar cells, antiferromagnetic materials, composite anodes for fuel cells, and chemical (gas) sensors. NiO is also examined, into that, for applications such as electrochemical devices, supercapacitors, smart windows, and dye-sensitive photocathodes [12].

The transparent glasses and ceramics doped with NiO have received interest for use in broadband optical amplifiers and tunable lasers due to its broad and extended emission in the wavelength spectrum covering the whole optical communication windows [13–15]. Both tetrahedral and octahedral positions in the glass network are occupied by nickel ions, when they are incorporated into base glass [16], and produce different colors depending on the equilibrium between nickel ions in the sixfold NiO_6 and fourfold NiO_4 coordination [17]. Ion concentration in the tetrahedral or octahedral positions is affected by the composition and type of the host glass [18].

Among others, the Broadband Dielectric Spectroscopy (BDS) has recently been considered as a very useful tool for probing charge carriers' transport as well as the different kinds of molecular dynamics in all condensed matters. This is because it can probe the molecular fluctuations and charge transport in broad ranges of frequency and temperatures.

Nickel oxide plays a very well role in traditional glasses in small amounts. Earlier researchers [19–21] investigated the optical, redox (Ni/Ni^{2+}), and magnetic properties of nickel-contained glasses with low NiO contents. Also, Smith et al. [22] used neutron diffraction to investigate the structural characterization of bioactive glasses doped with 4.0 mol% NiO and found Ni–O–Si bonding in the silicate network, with one third of the Ni^{2+} ion occupying a network forming tetrahedral geometry and the other two thirds occupying a fivefold coordination in the bio-glass. Finally, Suresh et al. [23] studied the spectroscopic characteristics of lead–bismuth–silicate glasses containing 0–1.0 mol. % NiO and found that Ni^{2+} ions were present in the glass in both octahedral and tetrahedral symmetries. According to the authors, increasing the concentration of Ni^{2+} ion increased its octahedral coordination, which dominated the tetrahedral coordination of Ni^{2+} ion in the glass. Because

of the importance of Ni²⁺ ions, we focused our research on the effects of major quantities of NiO could hardly be found in the literature on the structural, optical, and dielectric properties of calcium lithium silicate glasses and the Ni²⁺ environment in the glass matrix.

2 Materials and method

2.1 Glass synthesis

For the present investigation, the chemical composition of the glasses, based on (11.5 – x) CaO – 23.5 Li₂O – 65 SiO₂ (mol. %) was studied with NiO/CaO replacements (x NiO, where; 0 ≤ x ≤ 11.5). For this purpose, ACS Reagent Grades, Li₂CO₃ (99.0%), calcium carbonate (≥ 99.0%), nickel oxide powder (99.7%), and SiO₂ (99.9%) were used. All reagents were from Sigma Aldrich and used as received.

The glass samples were processed by the melt-quenching method. Where, the appropriate quantities of Li₂CO₃, CaCO₃, NiO, and SiO₂ solid reagents were completely mixed in an agate mortar. Each mixture was, then, liquefied in an alumina crucible in the 1275 °C – 1350 °C temperature range in an automatic temperature-controlled furnace for nearly 2 h. The formed free transparent liquid glass melts were, then, cast in a brass mold and successively annealed at 400 °C in a muffle furnace to relieve the structural stress.

Finally, each sample was cut into the desired shapes and sizes and polished for further characterization. The details of the glass composition samples and their labeling are given in Table 1. A photo of the prepared glasses containing NiO is shown in Fig. 1.

Table 1 Chemical composition of lithium calcium silicate glasses containing NiO

Glass samples	Chemical compositions (mol. %)			
	Li ₂ O	CaO	NiO	SiO ₂
GN0	23.5	11.5	–	56
GN1	23.5	8.63	2.87	56
GN2	23.5	5.75	5.75	56
GN3	23.5	2.87	8.63	56
GN4	23.5	–	11.5	56

2.2 Characterization techniques

The XRD patterns of the powdered glass samples were recorded by a Bruker-AXS D8 Advance diffractometer with Cu/Kα radiation (λ = 1.5406 Å) and Ni filtered at 0 < 2θ < 80, and 35 mA and 45 kV as generator settings with step size [· 2Th. = 0.0530].

For describing material tightening and structural changes of our samples, density (ρ) measurements were required. The Archimedes principle was employed to determine the densities, using distilled water as the immersion liquid [24].

$$\rho = \left\{ \frac{W_1}{W_1 - W_2} \right\} \times \rho_{\text{water}}, \quad (1)$$

where W₁ and W₂ denote the sample's weight in air and distilled water, respectively, and ρ_{water} denote the density of deionized water at room temperature (1.0 g/cm³). From the measured densities, the molar volume (V_m) of the studied samples was calculated using Eq. (2):

$$V_m = \sum x_i M_i / \rho, \quad (2)$$

where x_i is the molar fraction, M_i is the molecular weight of each (i) component and ρ is the sample density [25]. Table 1 shows the measured molar volume and density values. Density (ρ), molar volume (V_m), and other physical parameters like ionic concentration (N), polaron radius (r_p), and inter ionic distance (r_i) are estimated using the measured values.

A Vickers microhardness test was performed using (a SHIMADZU, HMV-2) instrument, adopting a 0.1 kg load on a flat glass surface. For all samples, the loading time was set to 20 s. Hardness values were recorded as an average of at least five indentations for each sample. The Vickers microhardness value (H_v) was determined using the following formula:

$$HV(Kg/mm^2) = A(P/L^2), \quad (3)$$

where A represents a geometrical constant equal to 1854.5, P is the applied load (g), and L is the average diagonal length (mm). By multiplying the obtained values by a constant value of 9.807, the values were converted from kg/mm² to MPa.

Fourier transform infrared absorption spectra (FTIR) were recorded at room temperature in the wavenumber region of 400 – 4000 cm⁻¹ by an infrared spectrophotometer (JASCOFTIR-430, Japan). Each sample has been mixed with KBr at a weight ratio of

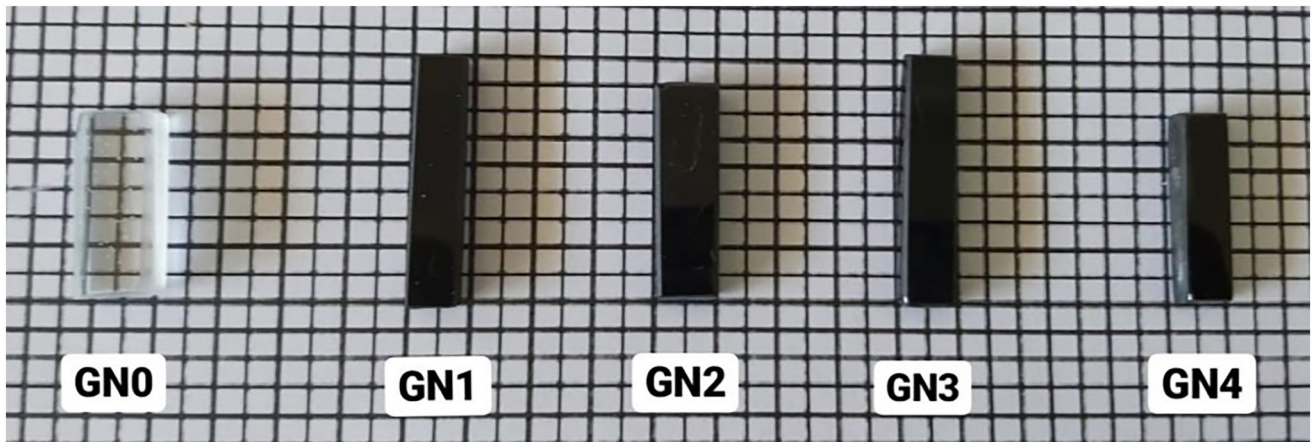


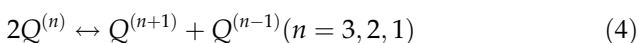
Fig. 1 Photo of the synthesized glass samples

1:100 before being pressed into a homogenous pellet. To eliminate moisture, the infrared absorbance measurements were performed at room temperature and shortly after producing the pellets.

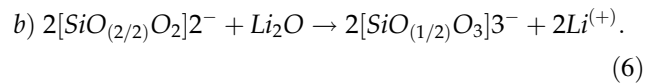
The diffuse reflectance spectra (DRS) of the samples have been studied from 300 to 2500 nm by the JASCO UV-VIS-NIR Spectrophotometer model V-670. The conductivity and dielectric parameters were performed using a high-resolution alpha analyzer (Novocontrol Technologies, GmbH & Co. KG). The measurements were carried out over a broad range of frequency [0.1 Hz–20 MHz] and isothermally at different temperatures ranging from 35 to 150 °C. The measuring temperature is stabilized with an accuracy of ± 0.1 °C using Quattro temperature controllers employing pure-nitrogen gas as the heating agent.

3 Results and discussion

Among different components of CaO – Li₂O – SiO₂ glass composition, SiO₂ is a well-known glass former that is predicted to collaborate in the glass matrix with tetrahedral [SiO_{4/2}]⁰ units, while the SiO₄ tetrahedral form shares all four oxygen atoms [26]. As demonstrated in the equilibrium process below, adding Li₂O (glass modifier) to silicate glasses causes the creation of non-bridging oxygens (NBOs) and other silicate structural groups inside the glass matrix.



The concentration of such structural units is affected by temperature, pressure, and the type of modifiers. The glass network is depolymerized by the Li⁺ ions via the equilibrium reactions mentioned below [27].



The coordination of Ni²⁺ causes many structural changes when nickel oxide is incorporated into these glasses. Nickel ions can be in a tetrahedral or octahedral coordination state. The glass network is generally affected by nickel ions with octahedral coordination together with calcium ions, resulting in a large number of non-bridging oxygen and interstitial impurity sites. Certain glass compositions may include nickel ions in the Ni²⁺ state. In glass systems, nickel cations prefer octahedral over tetrahedral sites in glass because octahedral environments have higher crystal field stabilization energy [28].

3.1 X-ray diffraction

The X-ray diffraction patterns of the selected glass samples (GN0, GN2, and GN4) are presented in Fig. 2. The obtained results show that the glasses have an amorphous structure and that there is no evidence of crystalline phases of the produced samples.

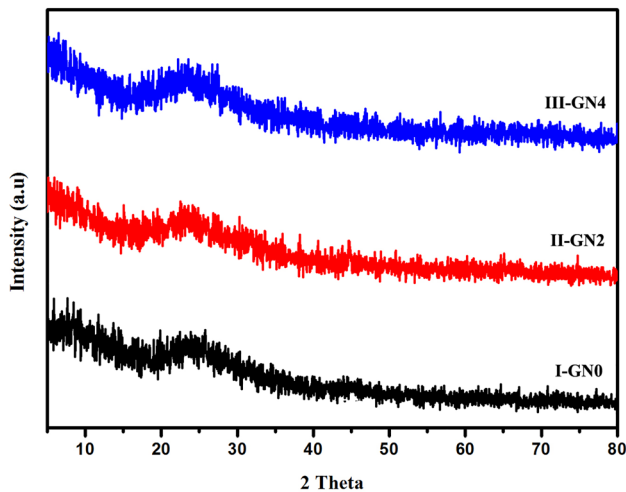


Fig. 2 XRD patterns of the selected glass samples (GN0, GN2, and GN4)

3.2 Physical properties

The density of the glass material is affected by factors such as structural compaction, changes in the glass matrix geometrical structure, changes in the glass forming ions coordination, and variations in the diameters of the interstitial holes. As a result, the density is proportional to how closely the ions and ionic units in the network are packed together. Figure 3 illustrates the correlation between density and molar volume in glass samples with different NiO contents. It is observed in Table 2 that the density of

prepared glasses is affected by the amount of NiO present. It was noted that the sample densities increased from 2.4794 to 2.6251 g/cm³, and the molar volume decreased from 21.1848 to 20.8251 cm³, respectively. The progressive density rise is due to the partial replacement of CaO with lower density (3.34 g/cm³) by NiO with higher density value (6.67 g/cm³). Furthermore, density can be increased by replacing higher molecular weight NiO (74.71 g/mol.) with lower molecular weight CaO (56.08 g/mol.) [29]. However, the molar volume of the glass matrix is reduced when CaO is replaced by NiO, resulting in compactness and rigidity.

The concentration of Ni²⁺ ions in the interior of the produced samples was determined using the formula:

$$N = \frac{\text{mol\%of dopant} \times \text{glass density} \times \text{Avogadro No.}}{\text{Average of glass molecular weight}} \quad (7)$$

The following relationships were applied to estimate the polaron radius (r_p), internuclear distance (r_i), and field strength (F).

$$r_p(\text{\AA}) = \frac{1}{2} \left(\frac{\pi}{6N} \right)^{\frac{1}{3}}, \quad (8)$$

$$r_i(\text{\AA}) = \left(\frac{1}{N} \right)^{\frac{1}{3}}, \quad (9)$$

Fig. 3 Relationship between density and molar volume of the prepared glasses

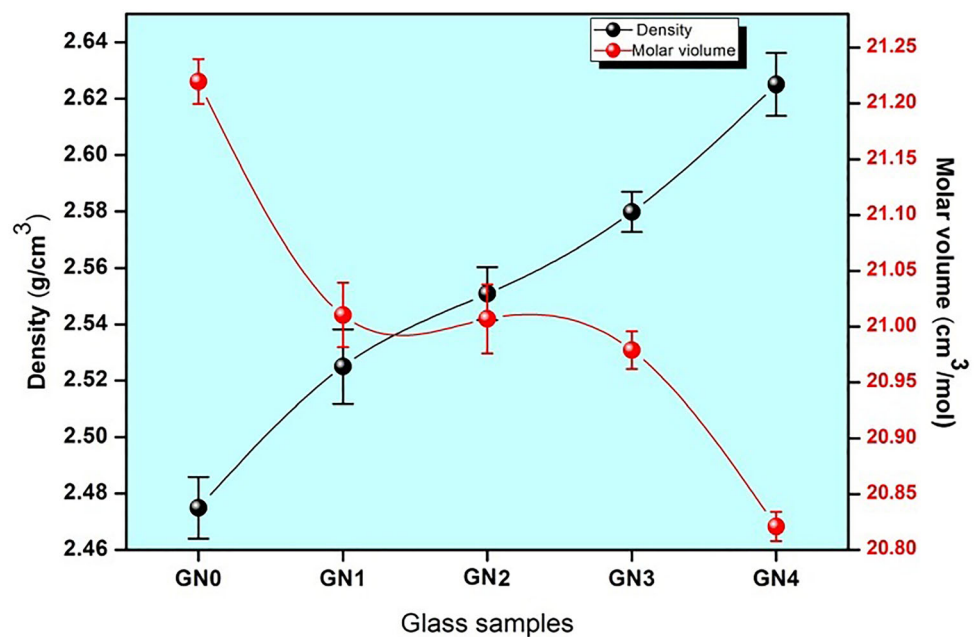


Table 2 Physical properties of the prepared glasses

Sl. no	Physical parameter (units)	Glass samples				
		GN0(x = 0)	GN1(x = 2.87)	GN2(x = 5.75)	GN3(x = 8.63)	GN4(x = 11.5)
1	Average molecular weight (g/mol)	52.5255	53.0602	53.5968	54.1333	54.6680
2	Density (ρ) (g/cm^3)	2.4749	2.5250	2.5509	2.5798	2.6251
3	Molar volume($cm^3/mole$)	21.1848	21.0140	21.0109	20.9835	20.8251
4	Microhardness(MPa)	4197	4428	4511	4536	4979
5	Ni^{2+} ion concentration (N) (10^{22} ions/ cm^3)	–	0.1645	0.3297	0.4954	0.6652
6	Inter-ionic distance (r_i) (Å)	–	8.4709	6.7191	5.8660	5.3172
7	Polaron radius (r_p) (Å)	–	3.4137	2.7078	2.3640	2.1428
8	F ($\times 10^{17} cm^{-2}$)	–	5.0357	8.0037	10.5025	12.7804
9	OPD(g. atm/l)	0.07789	0.07851	0.07853	0.07863	0.07923

$$F(cm^{-2}) = \frac{Z}{(r_p)^2}. \tag{10}$$

The oxygen packing density (OPD) in (g.atm/l) of glass was evaluated using the formula below, which indicates the distribution of oxygen atoms in the prepared glass network [29, 30]:

$$\text{Oxygen packing density} = 1000 \times O/V_m, \tag{11}$$

where ‘O’ denotes the presence of a number of oxygens in the oxide glass component and V_m is the molar volume. Table 2 contains the OPD values. This suggests that the glass structure is becoming more densely packed. Table 2 shows the measured physical properties of the investigated glasses as a function of Ni content. With increasing Ni^{2+} ion content, the oxygen packing density (OPD) and field strength (F) increase, indicating that structural characteristics improved [31]. As a result, the decrease in the values of internuclear distance (r_i) and polaron radius (r_p) with increasing dopant ion concentration (N) supported the rigidity of the glass structure [32].

Hardness is an important mechanical attribute of materials, which is described as a material’s resistance to scratching and indentation in a variety of situations [33]. Glass microhardness is a bond-sensitive property that indicates chemical bonding[34, 35]. As shown in Table 2, the prepared glass microhardness was determined and reported as 4197, 4428, 4511, 4536, and 4979 MPa for samples GN0, GN1, GN2, GN3, and GN4, respectively. It is clear that as the NiO content increased, microhardness increased dramatically. This increase could be attributed to the Ni^{2+} ion acting as a network intermediary

(tetrahedral and octahedral coordination), causing the glass structure to become more compact [36].

3.3 Fourier Transform Infrared Spectroscopy (FTIR) spectra

In general, FTIR analysis is a helpful non-destructive tool for evaluating compositional and structural changes of glass materials because it provides important information about the distribution of structural groups inside the glasses [37]. The effect of nickel oxide on the structural properties of the CaO–Li₂O–SiO₂ glass system was examined by obtaining FTIR spectra in the range of 400–1400 cm^{-1} , as shown in Fig. 4a. Because the record bands between 400 and 1400 cm^{-1} are wide and asymmetric, with the exception of a few shoulders, the experimental spectra must be performed (divided into their component bands). As a result of this deconvolution, all bands in the FTIR spectrum become more distinct, making it easier to identify their functions. Every component band in a structural group is associated with a specific type of vibration. Furthermore, individual component bands develop their own unique characteristics, such as a center associated with a specific type of bond vibration. In addition, the number of such bonds in a structural unit is related to its comparative area [38]. Several vibrational modes of the basic glass are depicted in Fig. 4b. The main characteristic of the silicate network is confirmed by the FTIR absorbance spectra bands of all the prepared glasses, possibly attributable to the presence of SiO₂ as a major constituent. The FTIR deconvolution spectrum for nickel-free glass (GN0) that was

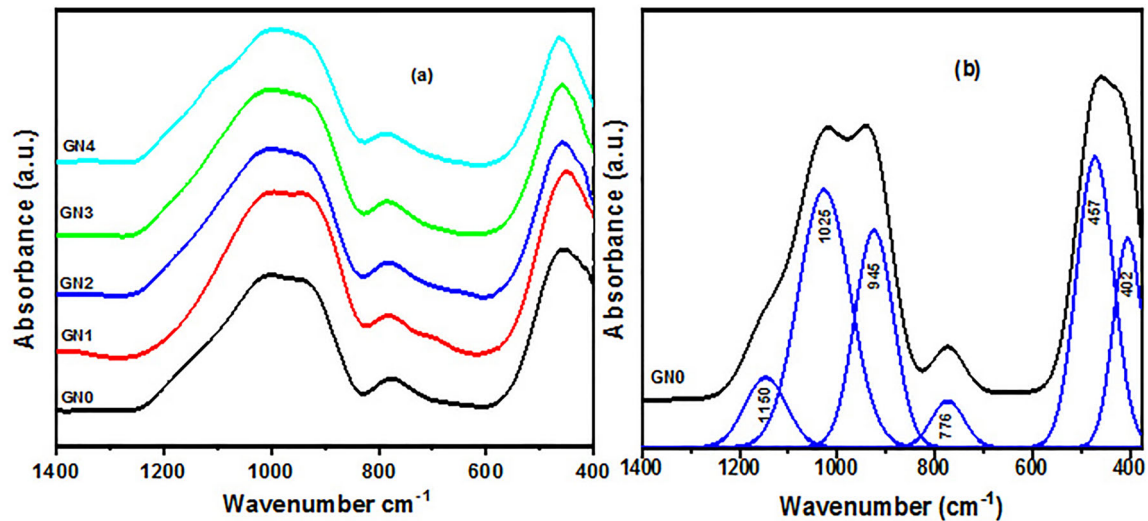


Fig. 4 **a** FTIR spectra of all studied glasses **b** Deconvoluted FTIR spectra of GN0 glass

obtained, in which $x = 0$ mol % NiO is presented in Fig. 4b. In this figure, the appearance of the following bands may be seen around ~ 402 , ~ 457 , ~ 776 , ~ 945 , ~ 1025 , and ~ 1150 cm^{-1} . The super position of many bands of the antisymmetric stretching vibration of the O–Si–O bonds of the SiO_4 tetrahedral units with different oxygen ions that form bridges or bonds is related to the wide, strong band at about 945–1150 cm^{-1} . The bands were attributed to Q^4 (four bridging oxygen ions), Q^3 (three bridging oxygen ions per silicon), Q^2 (two bridging oxygen ions), Q^1 (one bridging oxygen ion), and Q^0 (without bridging oxygen ions) of SiO_4 units, which are assigned in the 945–1150 cm^{-1} range [39, 40], whereas the band at 776 cm^{-1} was related to the Si–O–Si symmetric stretches of non-bridging oxygen atoms between tetrahedral. These regions can also have a band due to the distorted octahedral structure of NiO_6 . The bending/rocking vibrational band of Si–O–Si units was predicted in the 402–457 cm^{-1} spectral range. A stretching vibrational band due to Ni–O–Ni linkages is also expected in the 402–457 cm^{-1} spectral region. Because of the rocking/bending vibrations of the Si–O–Si units [1], this band appears to have merged with the other.

In addition, as the nickel oxide content in the glass matrix increases, IR spectra of the produced glasses reveal that all asymmetrical bands develop instead of symmetrical bands, and the Ni^{2+} ions appear to coexist in both 4- and 6-fold coordination in the current glass samples, and partially occupying the interstitial location. The transformation of Ni^{2+}

octahedral sites to tetrahedral sites causes the glass network to polymerize, resulting in a more compact glass structure. Table 3 shows the assignments of several band positions in the IR spectra.

3.4 UV–visible diffused reflectance analyses

Diffused reflectance spectroscopy (DRS) was employed to evaluate the optical properties of the prepared glass samples. The results are shown in Fig. 5a. The optical properties through DRS of the prepared glass samples indicate that absorption edge for nickel-free glass is observed at 236 nm, and for the initial substitution of NiO/ CaO, the absorption edge exhibited gradual red shift (shift longer wavelength), and for further increase of NiO content, the absorption edge exhibited gradual blue shift (shift longer wavelength). The energy bandgap of the samples has been determined using the Kubelka–Munk (KM) relation theory and is given in Eq. (12) [41].

$$F(R) = \frac{(1 - R)^2}{2R}, \quad (12)$$

where $F(R)$ denotes the Kubelka–Munk function and R denotes the percentage of reflectance. The plot between $(F(R)h\nu)^2$ and $h\nu$ gives the band-gap energies (E_g) of the studied glass samples as displayed in Fig. 5(b). For the investigated glass samples, the obtained optical band-gap energies were calculated to be 1.79, 1.82, 1.84, 1.86, and 2.01 eV, as shown in

Table 3 Summary of assignments of various bands in IR spectra of Li₂O–CaO–SiO₂:NiO glasses

Band(cm ⁻¹)	IR assignment	References
402–457	Asymmetric bending vibrations of SiO ₄ units stretching vibrational of Ni–O–Ni linkages	[26, 63]
776	Si–O symmetric stretching vibrations	[26, 64]
1100–1150	Asymmetric stretching vibrations of O–Si–O bonds in SiO ₄ tetrahedra with four bridging oxygen ions per silicon (Q ⁴)	[26, 64]
1050–1100	Asymmetric stretching vibrations of O–Si–O bonds in SiO ₄ tetrahedra with three bridging oxygen ions per silicon (Q ³)	[26, 64]
1000–1050	Asymmetric stretching vibrations of O–Si–O bonds in SiO ₄ tetrahedra with two bridging oxygen ions per silicon (Q ²)	[26, 64]
950–1000	Asymmetric stretching vibrations of O–Si–O bonds in SiO ₄ tetrahedra with one bridging oxygen ions per silicon (Q ¹)	[26, 64]
900–950	Asymmetric stretching vibrations of O–Si–O bonds in SiO ₄ tetrahedra without bridging oxygen ions per silicon (Q ⁰)	[26, 64]

Table 2. A slight increase in band-gap energy has been observed with increasing the NiO content. Incorporation of NiO in these glasses leads to several structural changes based on the coordination of nickel ions [28]. In tetrahedral coordination, it would enter the [SiO₄]⁴⁻ network as a [NiO₄]²⁻ species, but depending on the availability of oxygen in the environment, it might also act as a network modifier in octahedral coordination. The entrance of heavier Ni²⁺ ion as [NiO₄]²⁻ tetrahedral unites in substitution of lighter Si⁴⁺ ion in [SiO₄]⁴⁻ matrix caused the creation of Ni–O–Si links in the silicate network structure [29].

There are many variables to consider, including the refractive index (n), molar refraction (R_m), molar polarizability (α_m), and reflection loss (R_L) of the glasses that have been calculated by using equations [42, 43], and their values are provided in Table 4.

$$\left(\frac{n^2 - 1}{n^2 + 2}\right) = 1 - \sqrt{\frac{E_g}{20}}, \tag{13}$$

$$R_m = V_m \left[1 - \sqrt{\frac{E_g}{20}} \right], \tag{14}$$

$$\alpha_m = \left(\frac{3}{4\pi N_A}\right) R_m, \tag{15}$$

$$R_L = R_m / V_m. \tag{16}$$

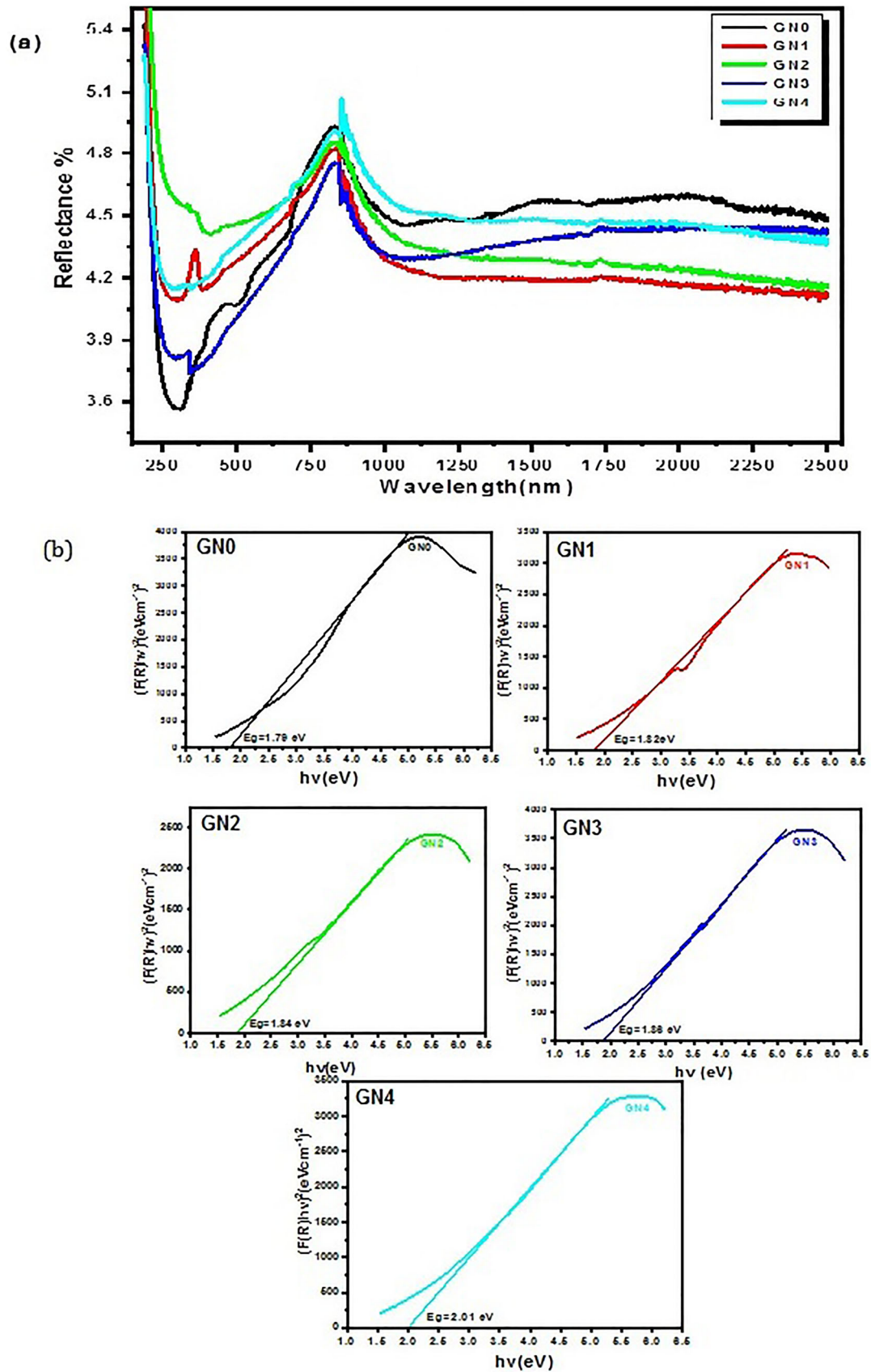
The refractive index of glass is a significant characteristic for elucidating the structure of glasses. It is dependent on the specific ions present in the glass besides the polarizability of the cations. The value of refractive index decreases, indicating that the number

of non-bridging oxygens decreases [43–45]. The molar refraction is the combination of the contributions of the oxygen ionic and cationic refractions [44]. With the addition of NiO, the molar refraction values decrease (Table 4). In the present glass samples, nickel ion appears to exist in both 4- and sixfold coordination and partially occupies the interstitial sites. In general, non-bridging oxygen ions are not formed by tetragonally positioned Ni²⁺ ions, whereas octahedrally positioned ions are, like any other transition metal ions in the glass network, may act as modifiers [46].

In most cases, the metallization criterion M is used to obtain information about the non-metallic entities of glass materials [47]. M values are completely dependent on R_L values, i.e., lower R_L values correspond to higher M values. It can also be used to explain the behavior of materials (insulator, semiconductor, and metallic). These M values are influenced by the materials refractive index and optical bandgap [48, 49]. The Dimitrov and Komatsu relation is used to calculate the M values of the prepared glasses, as in Eq. (17).

$$M = \sqrt{\frac{E_g}{20}}. \tag{17}$$

Essentially, If M has a large value, 1, a material is called an insulator, and if M has a small magnitude, it is called a metal [48, 49]. In our glasses, M values changed from 0.2990 to 0.3170, see Table 4. This means that M values are in between large values (insulators) and small ones (metals). As a result, the produced glasses function as semiconductors.



◀ **Fig. 5** **a** Diffuse reflectance spectra (DRS) of all the prepared glasses **b** band-gap energy measurements of all the prepared glasses

3.5 Dielectric and electrical investigations:

The complex permittivity [defined as $\epsilon^*(\nu) = \epsilon'(U) - i\epsilon''(\nu)$,] ϵ' is the real part, and ϵ'' is the imaginary part or dielectric loss, ($i = \sqrt{-1}$ and ν is the frequency), was obtained. The dissipation factor ($\tan \delta = \epsilon''/\epsilon'$), complex conductivity $\sigma^* = \sigma' + i\sigma''$, and electric modulus, $M^* = M' + iM''$ are determined and interpreted according to their interrelationships as detailed in Refs. [50–53]. The frequency dependence of the parameters: ϵ , $\tan \delta$, M'' , and σ' will be considered here. These three parameters are interrelated with each other according to

$$\epsilon^* = \epsilon' - i\epsilon'' = \frac{1}{i\omega Z^* C_0} = \frac{1}{M^*} = \frac{\sigma^*}{i\omega\epsilon_0}, \tag{18}$$

$$\tan\delta = \frac{\epsilon''}{\epsilon'}, \tag{19}$$

$$M = \frac{\epsilon}{\epsilon'^2 + \epsilon''^2}, \tag{20}$$

$$\sigma' = \epsilon_0\omega\epsilon'', \tag{21}$$

where ϵ_0 the permittivity of free space ($\epsilon_0 = 8.854 \times 10^{-12}$ As $V^{-1} m^{-1}$) and ω is the angular frequency ($\omega = 2\pi\nu$).

Figure 6 represents graphically the permittivity (ϵ') versus frequency at different temperatures for the NiO-free sample (GN0). Three different trends are noticed all over the frequency range under investigation. At the higher frequency range, starting from 20 MHz to about 100 kHz, the permittivity values are collapsed together and have nearly no effect, neither of frequency nor of temperature. This is due to the fact that at such higher frequencies, all fluctuations

and polarizations lag behind the alteration of the electric field. This agrees very well with what has been found recently [54, 55]. Further, a decrease in frequency shows a splitting out of the permittivity values with a remarkable effect of both temperature and frequency. The bend-like behavior in this case is originated from the well-known interfacial polarization. This phenomenon is supposed to be due to the space-charge polarization that developed at the grain boundaries. This kind of interfacial polarization generates a potential barrier, and therefore, the ions (cations and anions) accumulate at the grain boundaries. This interfacial polarization can be explained according to Maxwell–Wagner–Sillier (MWS-type) polarization that is usually found in the heterogeneous medium. The considered medium here contains conducting grains separated by grain boundaries of lower electrical conductivity just like a net of micro-capacitors [51, 52, 56, 57]. These bending is remarkably shifted towards higher frequencies (became faster) as the temperature increased

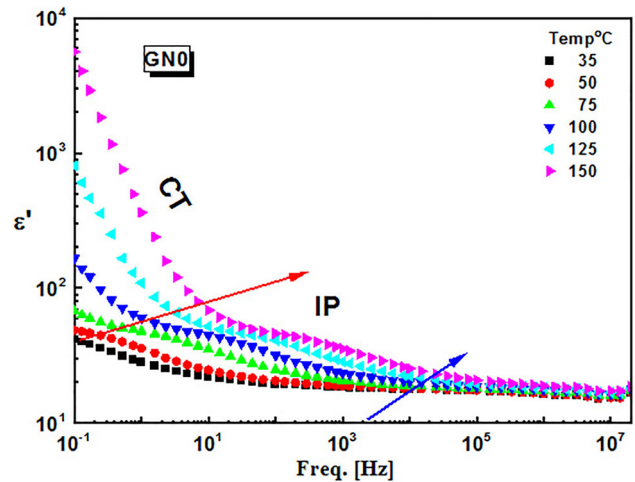


Fig. 6 Frequency dependence of permittivity, ϵ' , of the GN0 glass at indicated temperature

Table 4 Optical parameters of the glass samples for different NiO contents

Glass sample	Optical bandgap ($E_{opt.}$)(eV)	Refractive index (n)	Molar refraction R_m (cm^3/mol)	Molar polarizability $\alpha_m (\times 10^{22})$	Reflection loss (R_L)	Metallization criterion (M)
GN0	1.79	2.833	14.85	5.89	0.7010	0.2992
GN1	1.82	2.818	14.67	5.82	0.6981	0.3017
GN2	1.84	2.809	14.64	5.81	0.6968	0.3033
GN3	1.86	2.799	14.58	5.79	0.6948	0.3050
GN4	2.01	2.732	14.22	5.64	0.6828	0.3170

confirming the dynamic nature of the process. The lower frequency range shows a linear increase in permittivity, ϵ' , and hence of dielectric loss, ϵ'' (not shown here). The rate of change of ϵ' and ϵ'' increases remarkably as the temperature increases, confirming that the main response here is due to the charge transport (conductivity) which reduces the influence of any dynamic relaxation. This confirms the previously stated linear relationship between ϵ'' and electric conductivity in Eq. (21).

Figure 7 depicts the calculated loss tangent, $\tan \delta$, and electric-loss modulus, M'' as a function of frequency for three selected compositions, GN0, GN2, and GN4, as shown in Table 1. The space-charge polarization is appeared in these two parameters at higher frequencies than in the case of the permittivity spectrum. On the other hand, the peak shifted towards a lower frequency and its intensity became higher with the addition of nickel oxide. This may reflect the increase of the accumulated ions at the boundary accompanied by the slowness of their fluctuation. Several dielectric and electric-active processes can be detected as peaks in the modulus representation [50]. The frequency dependence of electric modulus loss shows that the conductivity contribution is converted into a peak. The conductivity peak is characterized by a lower density and a faster hopping mechanism (i.e., shifted towards higher frequency) as the calcium oxide is completely replaced by the nickel oxide. The space-charge

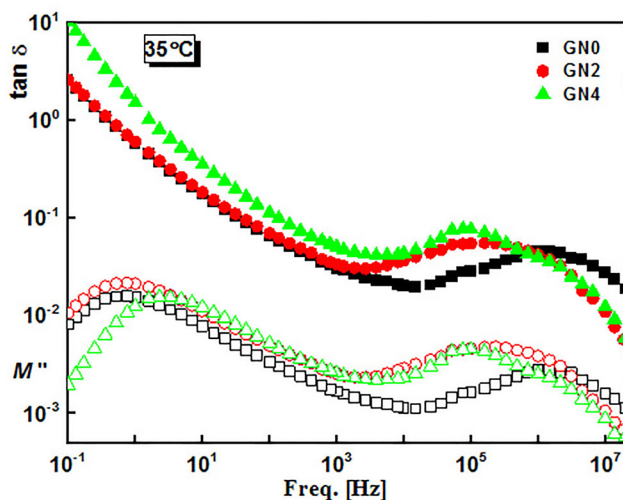


Fig. 7 Frequency dependence of the dissipation factor, $\tan \delta$ (closed symbols) and electric-loss modulus, M'' (open symbols) at 30 °C for the GN0, GN2, and GN4 glass samples at 35 °C

polarization separated remarkably in the modulus presentation and dissipation factor from the conductivity contribution peak. So, it appears in these two parameters at higher frequencies than in the case of the permittivity spectrum.

3.6 Electrical investigations

The charge carriers' transport process, and hence, the dc conductivity, σ_{dc} , is governed by the ability of the free ions to overcome the randomly distributed energy barriers. The highest energy barrier that must be overcome to achieve an infinite cluster of hopping sites determines the onset of dc conductivity [58]. The determined σ' and M'' are presented in Fig. 8 against frequency for the NiO-free sample as a representative example.

The real part of the complex conductivity (sometimes called ac conductivity), σ' , is characterized by a plateau-like behavior at the lower frequency range. This frequency-independent conductivity value determines the dc conductivity, σ_{dc} directly. The characteristic frequency, ν_c —at which dispersion sets in and turns into a power law at higher frequencies—is related to the hopping time [according to $\tau_h = 1/(2\pi\nu_c)$]. The conductivity spectrum represented here follows the empirical Jonscher power law very well [59, 60].

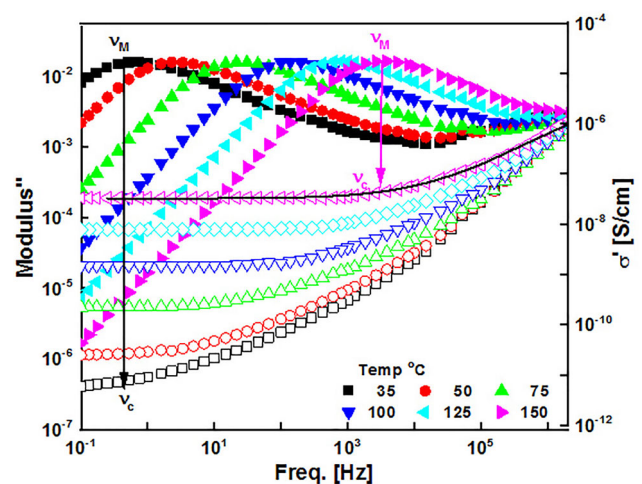


Fig. 8 Frequency dependence of the real part of complex conductivity, σ' (open symbols) and electric-loss modulus, M'' (closed symbols) of the GN0 sample at indicated temperatures. The line is fit of Eq. 22 to the data

$$\sigma'(v) = \sigma_{dc} \left[1 + \left(\frac{v}{v_c} \right)^n \right]. \tag{22}$$

The exponential n takes values between 0.5 and 1. Using Eq. 22, one can estimate both dc conductivity, σ_{dc} , and the characteristic frequency, v_c . These two parameters are related to each other according to the well-known empirical law of Barton–Nakajima–Namikawa, (BNN law): $\sigma_{dc} \sim v_c$. On the other hand, no decrease from σ_{dc} is noticed at lower frequencies, indicating the absence of any effect due to the electrode polarization. Figure 8 shows clearly the frequency position of the peak maximum of M'' as represented against frequency, (v_M) exactly at the same characteristic frequency, v_c , and shifted towards higher frequencies with heating at the same rate. This confirms that the dynamic peak on the electric modulus loss expresses the dynamic of the charge transport and, hence, the conductivity contribution. Empirically,

$$v_c \sim v_M \sim \frac{1}{2\pi\tau_h}, \tag{23}$$

with which v_M is the radial frequency corresponding to maximum peak position in the imaginary part of the electrical loss modulus. However, $v_c = (1/\tau_h)$ is the characteristic time that defines the attempt rate of the charge carrier to overcome the highest energy barrier that limiting the σ_{dc} , thereby enabling the physical interpretation of v_c within the random barrier model [61, 62]. Figure 8 represents the frequency dependence of the real part of conductivity, σ' , for the three selected samples at two different temperatures, namely, 35 °C and 150°C. The conductivity spectrum, $\sigma'(v)$, is dominated in the lower frequency range by the underlying physical mechanism of charge transport. The absolute values of dc conductivity deduced from the fitting of Eq. 22 to the data vary over more than 5 decades with temperature and upon systematic structural variation of the investigated composition. The temperature dependence of σ_{dc} , (semi-log scale), which is a directly observable quantity characterizing charge transport, consistent with the Jonscher equation (Eq. 22) is shown in the inset of Fig. 9. One has to conclude that, although the dc conductivity increases exponentially with temperature, the GN4 glass sample has the highest values all over the measuring temperatures. Similar behavior is found for the temperature dependence of the characteristic frequency, v_c , and modulus

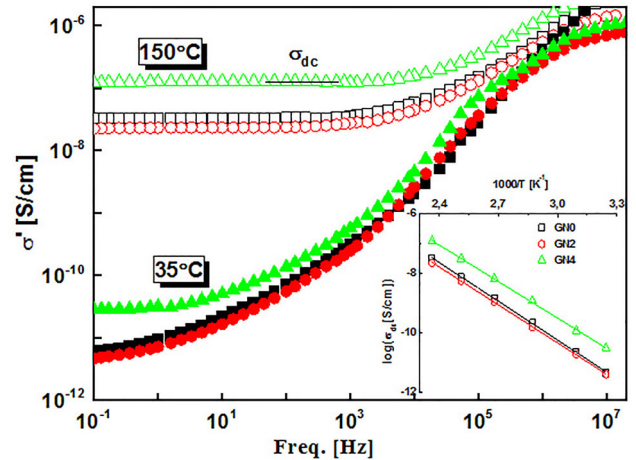


Fig. 9 Frequency dependence of the real part of complex conductivity, σ' : at 150 °C (open symbols) and at 35 °C (closed symbols) for the GN0, GN2, and GN4 glass samples. The inset shows the temperature dependence of the dc conductivity, σ_{dc}

frequency of the maximum position, v_M . This confirms, once again, the idea that the main topic in this range of frequency and temperature of the compositions under investigation are originated from the charge transport mechanism rather than the interfacial or any other fluctuations. The main two parameters characterizing charge transport, i.e., σ_{dc} and v_c , are directly observed during the fitting of Jonscher’s empirical equation to the data, which are graphically illustrated against each other (as shown in Fig. 10).

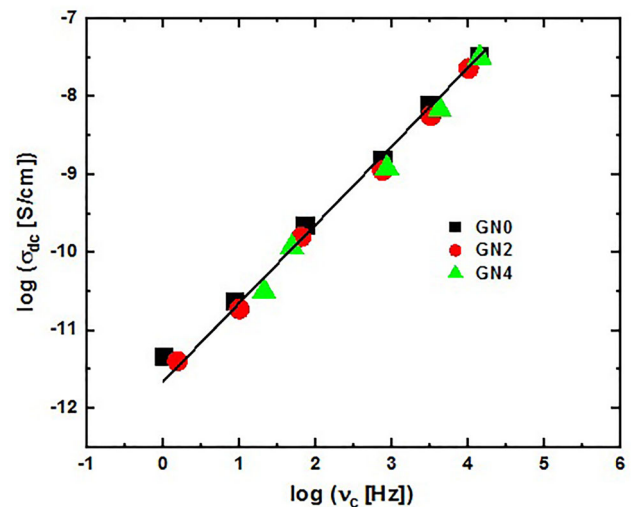


Fig. 10 The dc conductivity, σ_{dc} , as represented against characteristic frequency, v_c , for the GN0, GN2, and GN4 glass samples at different temperatures ranging between 35 °C and 150 °C. The solid line is a linear regression using all data points

BNN relationship holds for all the considered compositions and all the data collapse into one chart, indicating that the mechanism of charge transport is similar for all considered glasses.

4 Conclusions

A calcium lithium silicate glass system containing NiO was successfully synthesized. Furthermore, the structural, optical, and electric properties of the prepared glasses were also investigated. Powder X-ray diffraction patterns confirmed the glassy nature of all the prepared glass samples. Various physical properties of these glasses are examined. FTIR absorption spectra are characterized by intense absorption bands between 400 and 1400 cm^{-1} . Because of compositional variations, FTIR measurements have revealed structural changes in the glass matrix. Furthermore, with an increase in nickel oxide content, these results show the occurrence of octahedral Ni^{2+} ions at the expense of tetrahedral ions. The optical properties through DRS of the prepared glass samples indicate the existence of nickel ions both tetrahedral and octahedral positions. With increasing NiO content, a slight increase in optical band-gap energy has been observed, which is attributed to the Ni^{2+} would join the $[\text{SiO}_4]^{4-}$ network as $[\text{NiO}_4]^{2-}$ unites in tetrahedral coordination. Electrical investigations of the glass system show that the dc conductivity increases exponentially with an increase in temperature, and the relation between characteristic frequency and dc conductivity follows the empirical BNN model, and the mechanism of charge transport for the investigated samples is the same. The results suggest the semiconducting nature of glasses.

Funding

Open access funding provided by The Science, Technology & Innovation Funding Authority (STDF) in cooperation with The Egyptian Knowledge Bank (EKB).

Declarations

Conflict of interest The authors have no competing interests to declare that are relevant to the content of this article.

Open Access This article is licensed under a Creative Commons Attribution 4.0 International License, which permits use, sharing, adaptation, distribution and reproduction in any medium or format, as long as you give appropriate credit to the original author(s) and the source, provide a link to the Creative Commons licence, and indicate if changes were made. The images or other third party material in this article are included in the article's Creative Commons licence, unless indicated otherwise in a credit line to the material. If material is not included in the article's Creative Commons licence and your intended use is not permitted by statutory regulation or exceeds the permitted use, you will need to obtain permission directly from the copyright holder. To view a copy of this licence, visit <http://creativecommons.org/licenses/by/4.0/>.

References

1. G.R. Kumar et al., The role of Ni^{2+} ions on structural and spectroscopic properties of $\text{Li}_2\text{O}-\text{ZrO}_2-\text{Y}_2\text{O}_3-\text{SiO}_2$ glass system. *J. Non-Cryst. Solids* **498**, 372–379 (2018)
2. L. Feng et al., Optical properties of Ho^{3+} -doped novel oxyfluoride glasses. *J. Lumin.* **124**(2), 187–194 (2007)
3. A. Padmanabham et al., Spectroscopic and dielectric properties of crystallized $\text{PbO}-\text{Sb}_2\text{O}_3-\text{As}_2\text{O}_3$: NiO glass system. *J. Alloy. Compd.* **488**(1), 400–408 (2009)
4. B. Cochain et al., In situ local environment and partitioning of Ni^{2+} ions during crystallization of an oxyfluoride glass. *J. Non-Cryst. Solids* **408**, 7–12 (2015)
5. Murali Krishna, G., Y. Gandhi, and N. Veeraiah (2008), *Phys. Stat. Sol.*, **205**(1): p. 177–187.
6. G.S. Rao et al., Spectroscopic studies of lead arsenate glasses doped with nickel oxide. *J. Non-Cryst. Solids* **357**(3), 1130–1135 (2011)
7. V. Prasad et al., Dielectric dispersion, dipolar relaxation and ac conduction phenomena of NiO doped lead bismuth silicate glass system. *J. Non-Cryst. Solids* **500**, 460–467 (2018)
8. S. Zhou et al., Ligand-driven wavelength-tunable and ultra-broadband infrared luminescence in single-ion-doped transparent hybrid materials. *Adv. Func. Mater.* **19**(13), 2081–2088 (2009)
9. E.R. Beach et al., Solvothermal synthesis of crystalline nickel oxide nanoparticles. *Mater. Chem. Phys.* **115**(1), 371–377 (2009)

10. H.-L. Chen, Y.-M. Lu, W.-S. Hwang, Characterization of sputtered NiO thin films. *Surf. Coat. Technol.* **198**(1–3), 138–142 (2005)
11. H.H. Park, Efficient and stable perovskite solar cells based on inorganic hole transport materials. *Nanomaterials* **12**(1), 112 (2022)
12. K. Anandan, V. Rajendran, Morphological and size effects of NiO nanoparticles via solvothermal process and their optical properties. *Mater. Sci. Semicond Proc.* **14**(1), 43–47 (2011)
13. B. Johnson et al., Chemical durability, thermal stability and spectroscopic studies of the influence of Ni 2+ ions in oxyfluorophosphate glasses. *J. Mater. Sci.: Mater. Electron.* **27**(8), 8833–8847 (2016)
14. M.P. Rao et al., Copper ion as a structural probe in PbO–CaF₂–P₂O₅ glass system by means of spectroscopic and dielectric studies. *J. Alloy. Compd.* **472**(1–2), 489–496 (2009)
15. S. Yung et al., Concentration effect of Yb³⁺ on the thermal and optical properties of Er³⁺/Yb³⁺-codoped ZnF₂–Al₂O₃–P₂O₅ glasses. *Mater. Chem. Phys.* **117**(1), 29–34 (2009)
16. K.U. Kumar et al., Spectroscopic and 1.06 μm laser properties of Nd³⁺-doped K–Sr–Al phosphate and fluorophosphate glasses. *J. Alloy. Compd.* **458**(1–2), 509–516 (2008)
17. S. Khasa et al., Effect of nickel ions on electron paramagnetic resonance, DC conductivity and thermal behavior in vanadyl doped NiO·Li₂O·B₂O₃ glasses. *Mater. Chem. Phys.* **72**(3), 366–373 (2001)
18. M.M. Khalil et al., Optical and infrared absorption of gamma irradiated ternary silicate glasses containing NiO. *Indian J. Pure Appl. Phys.* **41**, 651–666 (2003)
19. R.S. Singh, S.P. Singh, *Phys. Chem. Glasses* **39**, 140–144 (1998)
20. R.S. Singh, S.P. Singh, Thermodynamic activity of nickel oxide in alkali silicate glasses. *Phys. Chem. Glass.* **40**(4), 235–241 (1999)
21. E.B. Pretorius, A. Muan, Activity of nickel (II) oxides in silicatemelts. *J. Am. Ceram. Soc.* **75**(6), 1490–1496 (1992)
22. J.M. Smith et al., Structural characterisation of hypoxia-mimicking bioactive glasses. *J. Mater. Chem. B.* **1**, 1296–1303 (2013)
23. B. Suresh et al., Spectroscopic features of Ni²⁺ ion in PbO–Bi₂O₃–SiO₂ glass system. *Spectrochim. Acta A Mol. Biomol. Spectrosc.* **141**, 263–271 (2015)
24. B. Jamalajah, GeO₂ activated tellurite tungstate glass: a new candidate for solid state lasers and fiber devices. *J. Non-Cryst. Solids* **502**, 54–61 (2018)
25. S.W. Hughes, Measuring liquid density using Archimedes' principle. *Phys. Educ.* **41**(5), 445 (2006)
26. B. Suresh et al., Spectroscopic features of Ni²⁺ ion in PbO–Bi₂O₃–SiO₂ glass system. *Spectrochim. Acta Part A Mol. Biomol. Spectrosc.* **141**, 263–271 (2015)
27. K.J. Rao, *Structural chemistry of glasses* (Elsevier, NJ, 2002)
28. R.K. Guntu, Luminescence and dielectric properties of Ni²⁺ ions added to calcio yttria borophosphate glasses for optoelectronic uses. *J. Lumin.* **209**, 258–266 (2019)
29. V.K. Vyas et al., Destructive and non-destructive behavior of nickel oxide doped bioactive glass and glass-ceramic. *J. Aust. Ceram. Soc.* **53**(2), 939–951 (2017)
30. V. Dimitrov, T. Komatsu, Classification of simple oxides: a polarizability approach. *J. Solid State Chem.* **163**(1), 100–112 (2002)
31. B. Bhatia et al., Optical basicity and polarizability of Nd³⁺-doped bismuth borate glasses. *New J. Glass. Ceram.* **5**(03), 44 (2015)
32. P. Pawar et al., Physical, thermal, structural and optical properties of Dy³⁺ doped lithium alumino-borate glasses for bright W-LED. *J. Lumin.* **183**, 79–88 (2017)
33. M.M. Smedskjaer, J.C. Mauro, Y. Yue, Prediction of glass hardness using temperature-dependent constraint theory. *Phys. Rev. Lett.* **105**(11), 115503 (2010)
34. Weeks, R. and J. Zarzycki, *Materials Science and Technology, A Comprehensive Treatment, Vol. 9, Glasses and Amorphous Materials.* by J. Zarzycki, VCH, Weinheim, 1991: p. 331–373.
35. S. Ibrahim et al., Preparation, physical, structural, optical characteristics, and gamma-ray shielding features of CeO₂ containing bismuth barium borate glasses. *J. Mater. Sci.: Mater. Electron.* **31**(22), 20060–20071 (2020)
36. A. Reichardt et al., Custom-made generation of three-dimensional nonwovens composed of polyglycolide or polylactide for the cardiovascular tissue engineering. *J. Biomater. Tissue. Eng.* **2**(4), 322–329 (2012)
37. S. Mansour et al., Impact of bismuth oxide on the structure, optical features and ligand field parameters of borosilicate glasses doped with nickel oxide. *Ceram. Int.* (2021). <https://doi.org/10.1016/j.ceramint.2021.04.154>
38. E. Mansour, FTIR spectra of pseudo-binary sodium borate glasses containing TeO₂. *J. Mol. Struct.* **1014**, 1–6 (2012)
39. N.O. Dantas et al., Effect of Fe₂O₃ concentration on the structure of the SiO₂–Na₂O–Al₂O₃–B₂O₃ glass system. *Spectrochim. Acta Part A Mol. Biomol. Spectrosc.* **81**(1), 140–143 (2011)
40. A. Akatov et al., Structure of borosilicate glassy materials with high concentrations of sodium, iron, and aluminum oxides. *Glass Phys. Chem* **35**(3), 245–259 (2009)
41. Aisida, S.O., et al., *Calcination induced PEG-Ni-ZnO nanorod composite and its biomedical applications.* *Materials Chemistry and Physics*, 2020. **255**: p. 123603.

42. J. Duffy, Chemical bonding in the oxides of the elements: a new appraisal. *J. Solid State Chem.* **62**(2), 145–157 (1986)
43. V. Dimitrov, S. Sakka, Electronic oxide polarizability and optical basicity of simple oxides I. *J. Appl. Phys.* **79**(3), 1736–1740 (1996)
44. S. Bhardwaj et al., Spectroscopic properties of Sm³⁺ doped lead bismosilicate glasses using Judd-Ofelt theory. *Spectrochim. Acta Part A Mol. Biomol. Spectrosc.* **117**, 191–197 (2014)
45. S.S. Sastry, B.R.V. Rao, Spectroscopic studies of copper doped alkaline earth lead zinc phosphate glasses. *Phys. B* **434**, 159–164 (2014)
46. G.M. Krishna et al., Characterization and physical properties of Li₂O–CaF₂–P₂O₅ glass ceramics with Cr₂O₃ as a nucleating agent—Physical properties. *J. Solid State Chem.* **180**(10), 2747–2755 (2007)
47. H. Morshidy, M. Sadeq, Influence of cobalt ions on the structure, phonon emission, phonon absorption and ligand field of some sodium borate glasses. *J. Non-Crystal. Solids.* **525**, 11966 (2019)
48. M. Farouk, Effect of Co²⁺ ions on the ligand field, optical, and structural properties of ZnLiB glasses. *Optik* **140**, 186–196 (2017)
49. V. Dimitrov, T. Komatsu, Electronic polarizability, optical basicity and non-linear optical properties of oxide glasses. *J. Non-Cryst. Solids* **249**(2–3), 160–179 (1999)
50. F. Kremer, A. Schönhal (eds.), *Broadband dielectric spectroscopy* (Springer Science Business Media, Heidelberg, 2002)
51. M.A. Mahdy, I. El Zawawi, G.M. Turkey, Lead telluride nanocrystalline thin films: Structure, optical characterization and a broadband dielectric spectroscopy study. *Curr. Appl. Phys.* **19**(7), 787–793 (2019)
52. F.H. Margha, G.T. El-Bassyouni, G.M. Turkey, Enhancing the electrical conductivity of vanadate glass system (Fe₂O₃, B₂O₃, V₂O₅) via doping with sodium or strontium cations. *Ceram. Int.* **45**(9), 11838–11843 (2019)
53. A. Abouhaswa, Y. Rammah, G.M. Turkey, Characterization of zinc lead-borate glasses doped with Fe³⁺ ions: optical, dielectric, and ac-conductivity investigations. *J. Mater. Sci.: Mater. Electron.* **31**(19), 17044–17054 (2020)
54. Turkey, G., et al., *Effect of Yttrium Oxide in Hydroxyapatite Biocomposite Materials: Electrical and Antimicrobial Evaluation*. ECS Journal of Solid State Science and Technology, 2021.
55. S.H. Gu et al., Complete genome sequence and molecular phylogeny of a newfound hantavirus harbored by the Doucet's musk shrew (*Crocidura douceti*) in Guinea. *Infect. Genet. Evol.* **20**, 118–123 (2013)
56. H. Abomostafa, G. El-Komy, G. Turkey, Microstructure and dielectric study of pure BST and doped BSTF ceramic materials by broadband dielectric spectroscopy. *Curr. Appl. Phys.* **20**(5), 611–618 (2020)
57. A. Fayad et al., Influence of CuO on crystallization and electrical properties of B₂O₃-Bi₂O₃-GeO₂-CaF₂ glass system for thermoelectronic applications. *J. Non-Crystal Solids.* **544**, 120185 (2020)
58. H. Böttger, V. Bryksin, *Hopping Conduction in Solids* (Akademie-Verlag, Berlin, 1985)
59. Jonscher, A.K., *The 'universal' dielectric response*. *nature*, 1977. **267**(5613): p. 673–679.
60. S.S. Omara et al., Hyperbranched poly (amidoamine)/kaolinite nanocomposites: Structure and charge carrier dynamics. *Polymer* **121**, 64–74 (2017)
61. J.C. Dyre, Source of non-Arrhenius average relaxation time in glass-forming liquids. *J. Non-Cryst. Solids* **235**, 142–149 (1998)
62. J.C. Dyre, Colloquium: The glass transition and elastic models of glass-forming liquids. *Rev. Mod. Phys.* **78**(3), 953 (2006)
63. M. Weber, R. Saroyan, R. Ropp, Optical properties of Nd³⁺ in metaphosphate glasses. *J. Non-Cryst. Solids* **44**(1), 137–148 (1981)
64. Morigaki, K., *Physics of amorphous semiconductors*. 1999: World Scientific.

Publisher's Note Springer Nature remains neutral with regard to jurisdictional claims in published maps and institutional affiliations.